Available online at www.sciencedirect.com
ScienceDirect
Trans. Nonferrous Met. Soc. China 33(2023) 2913−2925
Transactions of Nonferrous Metals Society of China
www.tnmsc.cn

Combining pre-rolling with retrogression and re-aging treatment to balance strength and corrosion resistance of 7A99 Al alloy

Tao ZHANG[1], Yu-zhu HOU[2], Biao-hua QUE[2], Yu-xin TIAN[3], Liang CHEN[2]

1. School of Mechanical Engineering, Nanjing Vocational University of Industry Technology, Nanjing 210023, China;
2. Key Laboratory for Liquid−Solid Structural Evolution and Processing of Materials (Ministry of Education), Shandong University, Jinan 250061, China;
3. School of Computer Science and Technology, Shandong Technology and Business University, Yantai 264005, China

Received 19 April 2022; accepted 27 September 2022

Abstract: The 7A99 Al alloy was subjected to peak aging (PA) and retrogression + re-aging (RRA), and the pre-rolling (R) was combined with RRA (RRRA) to balance the mechanical properties and corrosion resistance. The results show that the precipitates of PA-treated sample are mainly unstable η' phase with small size, while the coarse and stable η phase appears after RRA and RRRA. The grain boundary precipitates of PA-treated sample exhibit the smallest size and continuous distribution, while they show increased size, discontinuous distribution, and Cu enrichment after RRA and RRRA. The hardness and strength of RRRA-treated sample are higher than those of RRA-treated one, and they are even close to the values of PA-treated one. Moreover, the samples exhibit better corrosion resistance after RRA and RRRA than that after PA. These results indicate that the proposed RRRA method can enhance the corrosion resistance without a significant sacrifice on the mechanical strength.

Key words: 7A99 Al alloy; aging; pre-rolling; precipitates; mechanical properties; corrosion resistance

---

1 Introduction

The Al−Zn−Mg (7xxx series Al) alloys are extensively used in the fields of transportation, military equipment, and aerospace [1,2]. However, the application of 7xxx Al alloys is still restricted under some high load-bearing and harsh environmental conditions, considering the limits in mechanical strength and corrosion resistance. Hence, it is of great importance to improve both the strength and corrosion resistance of 7xxx Al alloys.

The peak aging (PA or T6) is a primary heat treatment method for 7xxx Al alloys [3,4], and it usually brings a remarkable strengthening effect attributed to the highly dispersed precipitates of metastable GP zone and η' ($MgZn_2$) phase [5]. However, PA is accompanied by the high susceptibility on stress corrosion cracking (SCC) [6,7]. The over aging (OA) can effectively enhance the SCC resistance, while it reduces the strength by 10%−15% in comparison with PA [8]. In order to balance the mechanical and SCC performances of 7xxx Al alloys, the retrogression and re-aging (RRA) treatment was developed [9]. The designing thought of RRA is that the GP zone and η' phase partially dissolve during the retrogression process, and then the η ($MgZn_2$) phase re-precipitates and grows along the grain boundaries (GBs) during the subsequent re-aging stage [10]. WANG et al [11] reported that RRA treatment could improve the tensile properties and conductivity of 7xxx Al alloy. WANG et al [12] applied RRA treatment on 7085 Al alloy, and found

---

Corresponding author: Biao-hua QUE, Tel: +86-531-81696577, E-mail: quebiaohua@mail.sdu.edu.cn;
Yu-xin TIAN, Tel: +86-535-6916191, E-mail: tianyuxin2006@sina.com

DOI: 10.1016/S1003-6326(23)66307-1

that the corrosion depth of RRA-treated sample was decreased by 70% in comparison with that of the PA-treated sample. ZHANG et al [13] studied the effects of RRA treatment on Al−8.9Zn−2.6Mg−1.7Cu alloy, and found that the SCC resistance was improved due to the large inter-space of grain boundary precipitates (GBPs) and the uniform distribution of Cu and Mg elements in GBPs.

Besides, it is widely accepted that the pre-deformation before aging affects the precipitation behavior of 7xxx Al alloys. It has been reported that the pre-deformation can introduce massive amounts of dislocations, which act as the nucleation sites of precipitation and promote the precipitation kinetics [14,15]. CERESARA and FIORINI [16] applied a pre-strain prior to natural aging, and found that the precipitation hardening response on strength properties was reduced due to the annihilation of vacancies in dislocations. YUAN et al [17] studied the effects of pre-strain on the SCC susceptibility of Al−Zn−Mg−Cu alloy, and found that the SCC resistance was greatly improved due to the discontinuous and large inter-space of GBPs. WANG et al [18] conducted the pre-cold rolling and PA treatment, and both the strength and SCC resistance of 7050 Al alloy were improved. WANG et al [19] applied 5% pre-strain and two-step aging on 7050 Al alloy, and the same conclusions were achieved.

The recently developed 7A99 Al alloy has relatively high Zn and low Cu contents, and can be applied in the fields of weapon and transportation due to its ultra-high strength and toughness. In order to obtain a good balance between the mechanical and corrosion properties of 7A99 Al, a deep study on the aging method and precipitation mechanism is necessary. However, the effects of pre-deformation on the aging precipitation of 7A99 Al have not been clarified. In this study, 7A99 Al was subjected to PA and RRA treatments. Moreover, the pre-cold rolling was introduced prior to RRA, and a novel method called RRRA (rolling + RRA) was developed. The microstructure and precipitation behavior during aging were examined. The effects of PA, RRA and RRRA on the mechanical properties and corrosion resistance of 7A99 Al were examined. It is aimed to provide an effective and reasonable aging method to achieve a good combination of mechanical and corrosion performances of 7A99 Al.

2 Experimental

2.1 Material and experiment

The cylindrical 7A99 Al billet with a diameter of 66 mm and a height of 200 mm was used for extrusion, and the chemical compositions of 7A99 Al are Al−8.18Zn−2.18Mg−1.72Cu−0.11Zr (wt.%). Prior to extrusion, the billet and extrusion die were preheated to 420 °C, and the container was preheated to 400 °C. Then, the extrusion was carried out using a 400 t extruder, and the ram velocity was kept as 5.0 mm/s during the whole process. A plate shaped profile with a cross-section of 30 mm × 3 mm was obtained. The extruded plate was held at 480 °C for 1 h to finish the solution treatment, followed by a quick water-quenching. During the subsequent artificial aging, both PA and RRA were adopted, and the detailed parameters are listed in Table 1. As seen, PA was conducted at 130 °C for 12 h, while RRA was held at 120 °C for 24 h, and at 180 °C for 0.5 h (retrogression), and finally at 120 °C for 24 h (re-aging). In addition, in order to study the effects of RRRA treatment, a pre-rolling with a reduction of 10% was carried out before RRA treatment.

Table 1 Detailed parameters of PA, RRA and RRRA treatments

Treatment	Cold rolling	Solution	Aging
PA	–	(480 °C, 1 h) + Quenching	130 °C, 12 h
RRA	–	(480 °C, 1 h) + Quenching	(120 °C, 24 h) + (180 °C, 0.5 h) + (120 °C, 24 h)
RRRA	10% reduction	(480 °C, 1 h) + Quenching	(120 °C, 24 h) + (180 °C, 0.5 h) + (120 °C, 24 h)

2.2 Microstructure characterization

The microscopic morphology and second phases of the aged 7A99 Al alloy were observed by scanning electron microscope (SEM, 15 kV, JSM−7800F, JEOL, Japan) equipped with energy dispersive spectrometer (EDS, XMax-80, Oxford, UK). The precipitations were analyzed through transmission electron microscope (TEM, Talos F200S G2, Thermo Fisher, USA), high-resolution TEM (HRTEM), and high angle annular dark field scanning TEM (HAADF-STEM). The sample for

SEM observation was ground and polished without etching. The TEM sample was ground to have a thickness of 50 μm and twin-jet electropolished in a solution of 30% nitric and 70% methanol at −30 °C.

2.3 Mechanical and corrosion tests

The Vickers hardness was measured using a micro-hardness tester (HVS−1000A, Huayin, China) with a load of 4.9 N and a dwell time of 10 s. To achieve the average value, 5 positions were selected from each sample for hardness test. For tensile test, the sample with a gauge length of 25 mm was sectioned from the extruded plate along the extrusion direction (ED), and the detailed dimension is shown in Fig. 1(a). The tensile test was carried out on a testing machine (Exceed E45, MTS, China) at the ambient temperature. The stretching speed during tensile test was set to be 1.5 mm/min, and the strain was measured using a 25 mm clip gauge extensometer. In order to evaluate the corrosion behavior of 7A99 Al, the sample was immersed in the 3.5 wt.% NaCl aqueous solution to test the pitting corrosion resistance, and the area ratio of corrosion pits was calculated. The SCC behavior was evaluated by the slow strain rate test (SSRT), and the dimension of SSRT sample is shown in Fig. 1(b). The SSRT test was carried out under a strain rate of 1×10^{-6} s^{-1} on a testing machine (YYF 50, Bairoe, China). During SSRT test, the sample was exposed in the air and 3.5 wt.% NaCl aqueous solution, respectively.

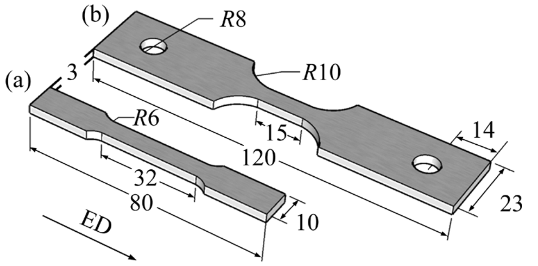

Fig. 1 Schematic diagram of samples of tensile test (a) and SSRT (b) (Unit: mm)

3 Results and discussion

3.1 Microstructure

The SEM images of PA, RRA and RRRA samples are shown in Fig. 2, where the chemical compositions of the secondary phases marked by arrows are listed in Table 2. The dark grey matrix and bright white second phases are observed in PA sample, as shown in Fig. 2(a). The EDS results in Table 2 indicate that the coarse spherical particle (Point 1) should be *S* phase (Al_2CuMg), and the granular particle (Point 2) with a smaller size is

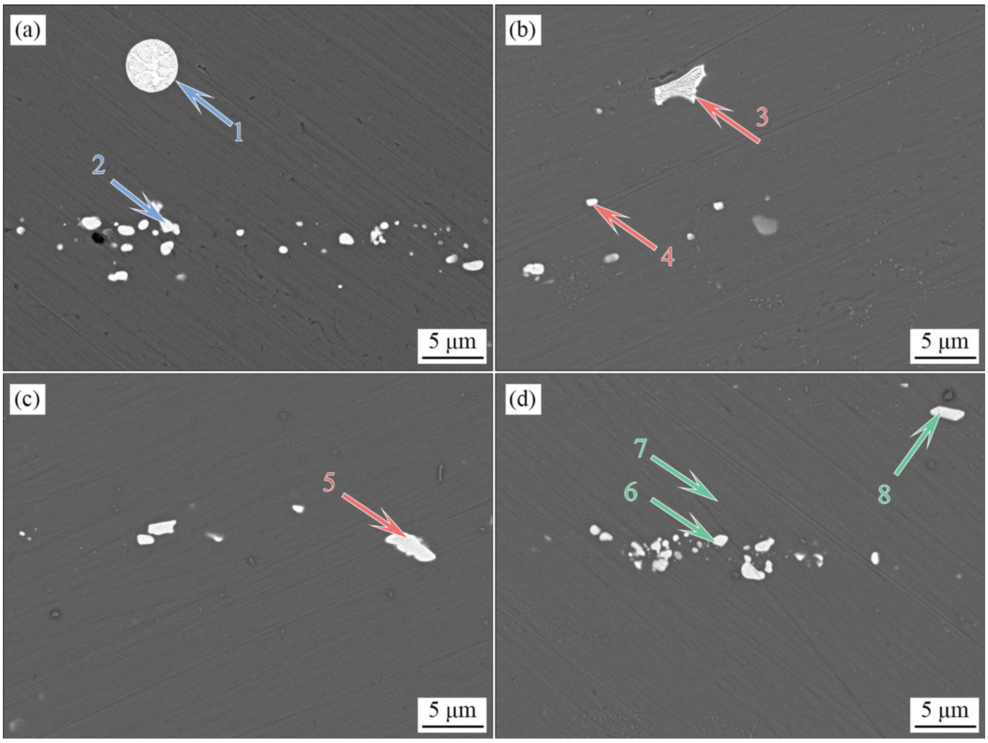

Fig. 2 SEM images of second phases of samples treated by PA (a), RRA (b, c), and RRRA (d)

Table 2 Chemical compositions of second phases indicated in Fig. 2 (at.%)

Point	Sample	Al	Zn	Mg	Cu	Fe	Phase
1	PA-treated	51.6	17.1	15.5	15.8	−	Al_2CuMg
2		65.5	0.7	0.2	20.1	13.6	Al_7Cu_2Fe
3	RRA-treated	58.1	14.4	16.4	11.1	0.1	Al_2CuMg+ $MgZn_2$
4		79.1	2.6	1.5	9.7	7.0	Al_7Cu_2Fe
5		65.8	0.6	0.3	19.2	14.1	Al_7Cu_2Fe
6	RRRA-treated	73.5	1.9	1.2	13.6	9.8	Al_7Cu_2Fe
7		92.3	4.0	2.7	1.0	−	$MgZn_2$
8		71.2	1.7	0.8	16.3	10.1	Al_7Cu_2Fe

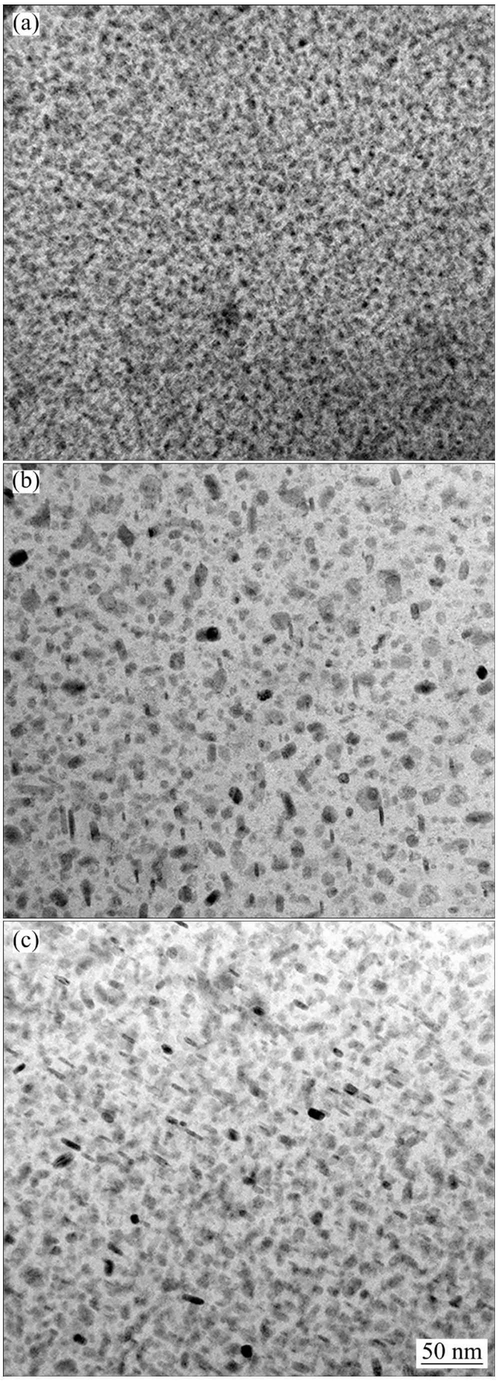

Fig. 3 BF TEM images showing morphology of precipitates inside grains of samples treated by PA (a), RRA (b), and RRRA (c)

identified as Al_7Cu_2Fe [20]. These two phases can also be found in RRA sample, as indicated by Points 3−5 in Figs. 2(b, c). It should be noted that the particle indicated by Point 3 exhibits a layer structure, which implies that it may be a multi-constituent eutectic. Based on the EDS data in Table 2, the eutectic is determined as Al_2CuMg and $MgZn_2$, and this kind of mixed phases were also reported in the previous study [21]. In RRRA sample, the second phases become relatively finer and the coarse phases are rare, which implies that the coarse phases might be broken by the pre-cold rolling process.

Figure 3 shows the bright-field (BF) TEM images about the distribution of precipitates. It is seen from Fig. 3(a) that the precipitates of PA sample own the smallest size and the most intensive distribution. An obvious increase of the precipitate size is observed in RRA sample, and the inter-space between them becomes large, as shown in Fig. 3(b). For RRRA sample, both the size and density of precipitates are in the middle level. In order to make a further investigation on the precipitates, the HRTEM images and the corresponding fast Fourier transform (FFT), inverse FFT (IFFT) patterns are presented in Fig. 4, and the selected area electron diffraction (SAED) images are shown in Fig. 5. As seen from Fig. 4(a), the precipitates in PA sample with an average radius of ~3 nm are densely dispersed, which is consistent with the results of Fig. 3(a). Combined with the SAED patterns in Figs. 5(a, b), it is clear that the main precipitates of PA are semi-coherent with the Al matrix, which implies that the precipitate should be η' phase [22]. As shown in Fig. 4(b), the quite coarse precipitates with an average radius of ~7 nm are observed in RRA sample. Based on the SAED patterns in Figs. 5(c, d), the precipitate of RRA should be η phase that is non-coherent with Al matrix. For RRRA sample, it is seen from Fig. 4(c) that the η' phase is still dominant and densely distributed, which is further confirmed by the very obvious η' phase spots in the SAED patterns of Figs. 5(e, f). It

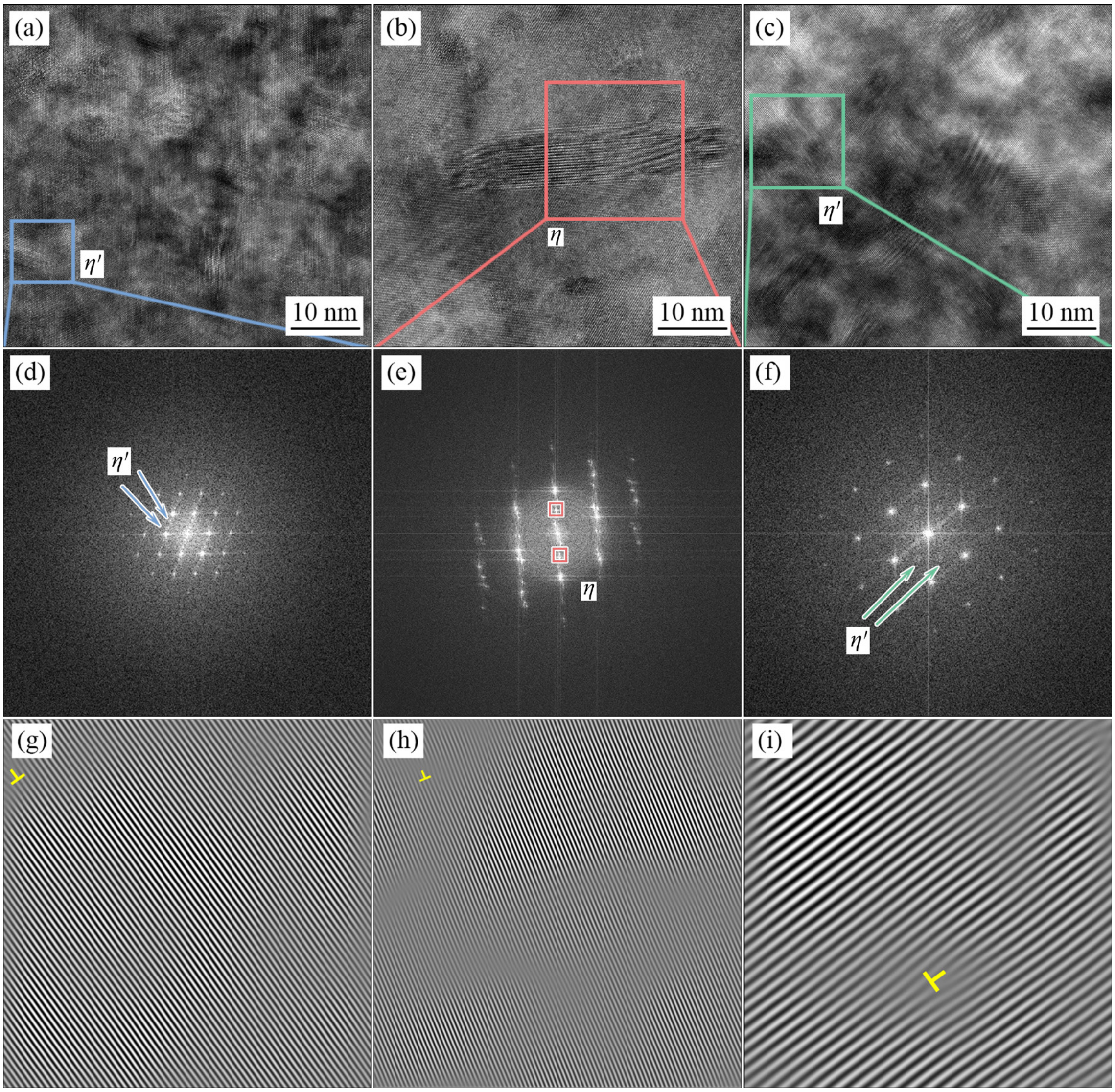

Fig. 4 HRTEM images along $\langle 110\rangle_{\mathrm{Al}}$ orientation of samples treated by PA (a), RRA (b), and RRRA (c); Reciprocal lattice of selected precipitates obtained by FFT of samples treated by PA (d), RRA (e), and RRRA (f); Lattice images of selected precipitates obtained by IFFT of samples treated by PA (g), RRA (h), and RRRA (i)

is noted that the weak spots of η phase are also observed in RRRA sample, as shown in Fig. 5(e). Interestingly, as displayed in Figs. 4(g−i), the dislocations all locate outside the precipitates, which indicates that the dislocations do not cut through the precipitates.

The type, size and distribution of the precipitates of different samples vary significantly, and the reasons are explained here. During the PA treatment, due to the relatively low aging temperature of 130 °C, most of the GP zones only transform into η' phase, and the transformation from η' phase to η phase is hard to take place. Moreover, since the aging time is only 12 h, the growth and coarsening of the precipitates are not obvious. In regard to RRA, the retrogression temperature is increased to 180 °C, and the metastable η' phase inside the grains partially or completely dissolves during the short-time retrogression. Then, η' phase re-precipitates to form the stable η phase and grows up to a certain extent during the subsequent re-aging process [10]. In the case of RRRA, the effects of pre-deformation are mainly manifested in two aspects. First, the introduced dislocations accelerate the diffusion of solute atoms, and thus the precipitation kinetics is promoted [23]. Second, the dislocation density inside the grain is greatly increased by pre-deformation, which provides the favorable heterogeneous nucleation sites and the required nucleation energy for η phase [24]. Hence,

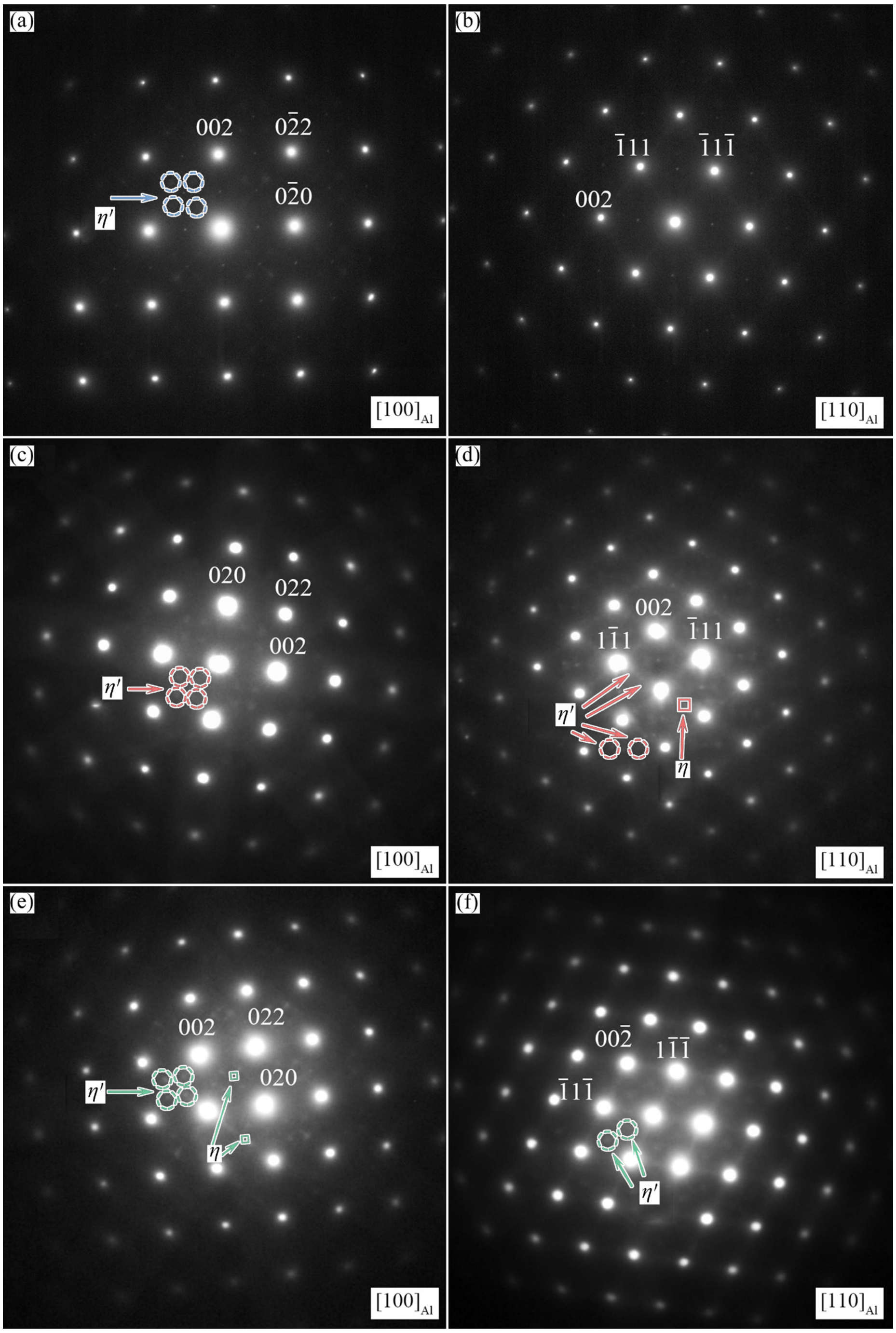

Fig. 5 SAED patterns of samples treated by PA (a, b), RRA (c, d), and RRRA (e, f) (Dotted circles represent η' phase, and the squares correspond to η phase)

the precipitate size of RRRA sample is smaller than that of RRA sample.

Figure 6 shows the BF TEM images at the GB of different aged samples. As seen from Fig. 6(a), the GBPs of PA sample have the smallest size with a continuous and dense distribution, and the width of precipitate free zone (PFZ) is only around 22 nm. When the alloy is subjected to RRA treatment, the GBPs are markedly coarsened, and the inter-space of precipitates as well as the PFZ width (~37 nm) are significantly increased, as shown in Fig. 6(b). This morphological feature was also reported by NANDANA et al [25]. Unlike the η' phase which dissolves during the retrogression stage, the GBPs cannot dissolve. In the subsequent re-aging stage, GBPs continue to coarsen due to the pre-existing particles, resulting in the wide PFZ [10]. For RRRA sample, the GBPs also exhibit a discontinuous distribution, as shown in Fig. 6(c). The size of GBPs and the width of PFZ (~25 nm) of RRRA sample both are larger than those of PA sample, but smaller than those of RRA sample. As mentioned above, the main reason is that the dislocations and vacancies are introduced by pre-rolling, and they offer additional and sufficient nucleation sites of precipitation.

In order to examine the element distribution, the HAADF-STEM images and the corresponding EDS results are shown in Fig. 7. It is seen that the precipitates of all aged samples mainly contain Al, Zn, Mg and Cu elements, among which Zn is obviously enriched in GBPs. As is known, the diffusion of solute atoms along GB is much faster than that in the matrix. Moreover, the diffusion of Zn and Mg is higher than that of Cu [26,27]. Hence, η phase with Zn and Mg elements preferentially precipitates at GB. During the subsequent growth of precipitate, since the solute atoms at GB are consumed more rapidly than those in the matrix, the solute atoms are continuously transported from the matrix to GB, which is driven by the reduction in GB energy [28]. As a result, PFZ is formed adjacent to GB, and GBPs are larger compared to the matrix precipitates. As shown in Fig. 7, the Cu enrichment of GBPs of PA sample is not observed, while it is obvious in the GBPs of both RRA and RRRA samples. Based on the EDS analysis, it is known that the contents of Cu atoms of PA, RRA and RRRA samples are 1.60, 3.84, and 2.77 at.%, respectively. This implies that RRA leads to the Cu

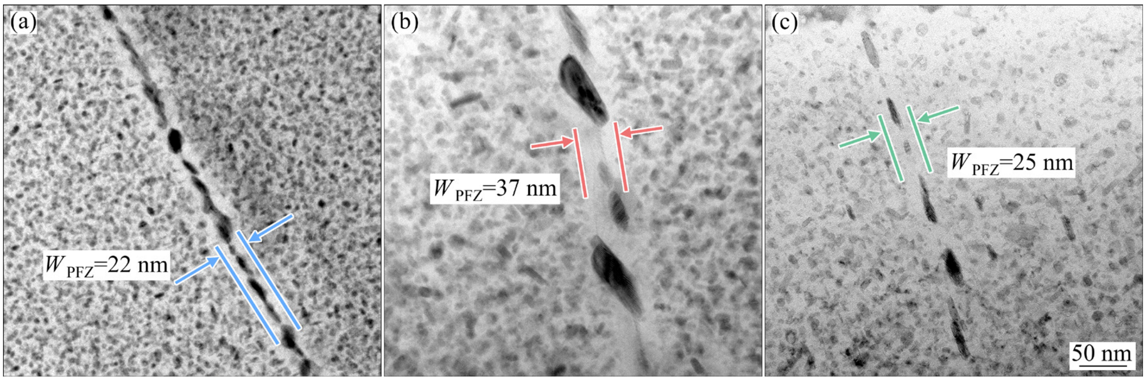

Fig. 6 BF TEM images showing GBPs of samples treated by PA (a), RRA (b), and RRRA (c)

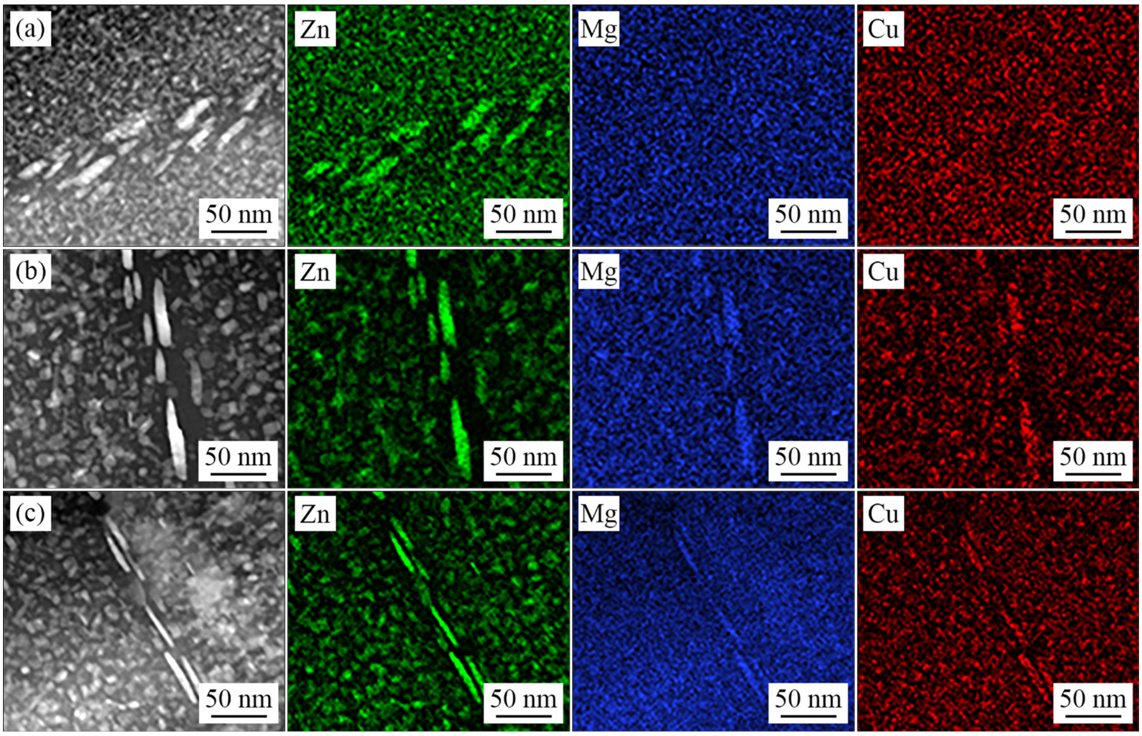

Fig. 7 HAADF-STEM micrographs and elemental distribution mappings of Zn, Mg and Cu of samples treated by PA (a), RRA (b), and RRRA (c)

enrichment of GBPs. According to the first-principle calculation reported by FANG et al [29], when the Zn atoms of η phase are replaced by Cu atoms, the formation enthalpy of the structure decreases, which enables the segregation of Cu at GBPs. Hence, due to the longer aging time of RRA and RRRA treatments, the Cu enrichment of GBPs is more obvious.

3.2 Vickers hardness

The hardness of PA, RRA and RRRA samples are displayed in Fig. 8. As is shown, the RRA sample owns the lowest hardness of HV 178, while the PA sample achieves the highest hardness of HV 195. The hardness of RRRA sample is about HV 192. In general, the variation of hardness is related to the work hardening, aging precipitates, and other factors. As shown in Fig. 3, the precipitates of PA sample have the smallest size and the densest distribution, and the strong precipitate strengthening leads to the highest hardness. The reduction of hardness of RRA and RRRA samples is attributed to the increasing size of precipitates. Moreover, as shown in Fig. 9(a), it is difficult to find the dislocations inside the RRA sample. In terms of RRRA sample, although the solution is carried out at an elevated temperature of 480 °C for 1 h, lots of dislocations are remained, as shown in Fig. 9(b). This fact indicates that the work hardening effect introduced by pre-rolling is not fully released by the high temperature solution. Hence, due to above two reasons, the hardness of RRRA sample is much higher than that of RRA sample, and it is even close to the hardness of PA sample.

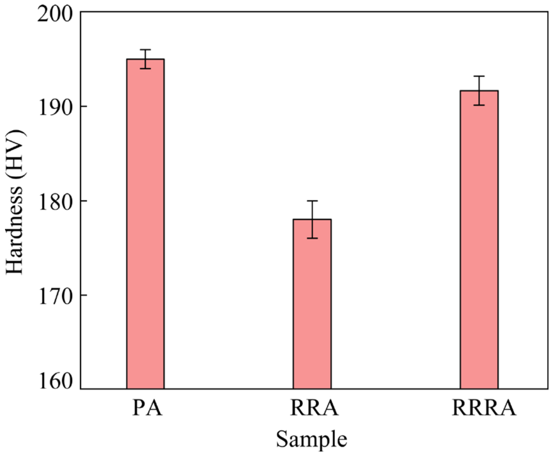

Fig. 8 Hardness of samples treated by PA, RRA and RRRA

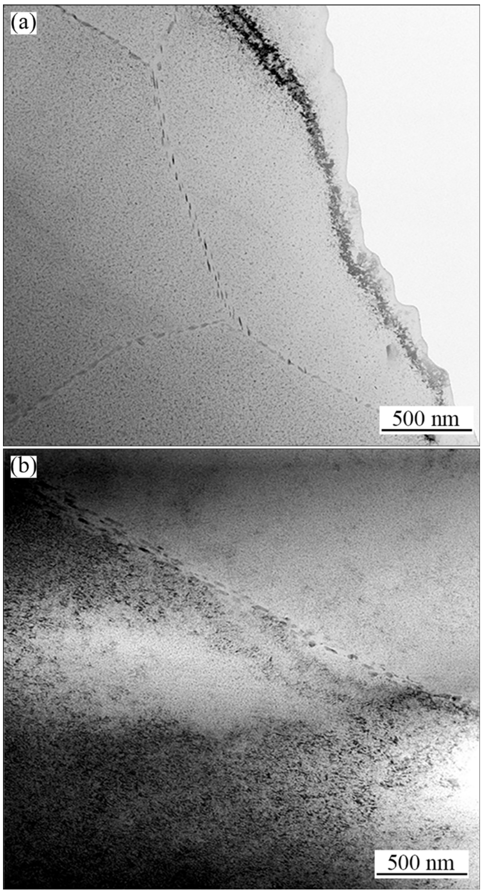

Fig. 9 BF TEM images showing dislocation distribution of samples treated by RRA (a) and RRRA (b)

3.3 Tensile properties

Table 3 lists the yield strength (YS), ultimate tensile strength (UTS), and elongation obtained from the tensile tests. The YS and UTS values of PA sample are respectively 621 and 668 MPa, which are both higher than those of RRA and RRRA samples. Due to the contribution of pre-rolling, RRRA sample has higher YS and UTS values than RRA sample. The YS and UTS of RRRA sample are respectively 596 and 655 MPa, which are even close to those of PA sample. In terms of the elongation, PA sample has the lowest value of 10.5%, which is less than 11.8% of RRA sample and 11.3% of RRRA sample.

Table 3 YS, UTS and elongation of different samples

Sample	YS/MPa	UTS/MPa	Elongation/%
PA-treated	621	668	10.5
RRA-treated	582	630	11.8
RRRA-treated	596	655	11.3

In order to further analyze the relationship between the microstructure and tensile properties, YS is described by the following formula:

$$\sigma_y=\sigma_i+\sigma_d+\sigma_{sol}+\sigma_p \tag{1}$$

where σ_y is the the overall YS, σ_i is the YS of pure Al and it is usually considered to be 10 MPa [30,31], σ_d is the strength contributed by dislocation, σ_{sol} is the strength contributed by solid solution, and σ_p represents the strength contributed by precipitates.

Since the dislocation tangles create obstacles to the movement of dislocation, the dislocation contribution can be estimated based on Eq. (2) [32]:

$$\sigma_d=M\alpha\mu b\sqrt{\rho_d} \tag{2}$$

where M is the mean orientation factor of 3, α is a constant of 0.27, μ is the matrix shear modulus (~26.9 GPa), b is the magnitude of Burgers vector which equals 0.286 nm for FCC Al [31], and ρ_d is the dislocation density. Hence, the value of σ_d has positive correlation with the dislocation density ρ_d. That is to say, the more the dislocations are, the greater strengthening effect is. In this study, the dislocations are introduced into RRRA sample by pre-rolling, and large amount of dislocations still remain after a series of solution and aging treatments, as shown in Fig. 9(b). Consequently, a strong dislocation strengthening is achieved in RRRA sample.

The contribution of the solid solution strengthening can be expressed by Eq. (3) [33−35]:

$$\sigma_{sol}=M\mu b\varepsilon_{sol}^{3/2}\sqrt{c} \tag{3}$$

where ε_{sol} is the lattice strain caused by the difference in atomic radii between the solute (Zn, Mg and Cu atoms) and solvent atoms (Al atoms) and the strengthening effect tends to increase with the increase of ε_{sol} value, and c is the element concentration. Assuming that all atoms are in solid solution, the YS enhancement of Zn, Mg and Cu elements are 2.9, 18.6 and 13.8 MPa/wt.% [35], respectively. Referring to the element content of the 7A99 Al alloy, the theoretical contributions of Zn, Mg and Cu to YS are 23.7, 40.5, 23.7 MPa, and 87.9 MPa in total. It should be noted that not all Zn, Mg and Cu atoms are in solid solution because of the precipitates during the aging treatment. Thus, the actual contribution by element is less than the theoretical value, which is a relatively small contribution to the YS.

Generally, the dispersed precipitated phases play a key role in hindering the movement of dislocations. Since there is no dislocation cutting through the precipitates is seen from Figs. 4(g−i), the operative strengthening mechanism is likely to be dislocation by-passing, which can be expressed by Orowan equation [35]:

$$\sigma_p=M\frac{0.4\mu b}{\pi\sqrt{1-v}}\frac{\ln(2\overline{r}/b)}{\lambda_p} \tag{4}$$

where v is the Poisson ratio of 0.33. For a spherical precipitate, $\overline{r}$ is equal to $\sqrt{2/3r}$, where r is the average radius of all precipitates. λ_p is the mean edge-to-edge interprecipitate spacing, which can be calculated from the radius $\overline{r}$ and volume fraction (f) of the precipitates as follows [36]:

$$\lambda_p=\left[\left(\frac{3\pi}{4f}\right)^{1/2}-1.64\right]\overline{r} \tag{5}$$

Based on Eqs. (4) and (5), it is known that the precipitation strengthening σ_p is positively correlated with the volume fraction f of precipitates. Moreover, the size of most precipitates discussed in this study is larger than 3 nm, and σ_p has negative correlation with the radius r of precipitates. The volume fractions of precipitates of PA, RRRA and RRA samples are respectively 5.73%, 2.87% and 2.32%, which were calculated based on the methodology reported in Ref. [22]. In addition, the precipitate size follows the order of PA < RRRA < RRA samples. Hence, the precipitation strengthening is strong in PA sample, while it becomes weak in RRRA and RRA samples. In a word, because of the synergistic effects of dislocation strengthening, solution strengthening and precipitation strengthening, PA sample owns the highest strength and RRA sample owns the lowest strength.

3.4 Corrosion behavior

The aged samples were immersed in 3.5 wt.% NaCl solution for 24 h at room temperature, and the corroded surfaces are shown in Fig. 10. The corrosion pits and second phases are clearly seen on the surfaces of all samples. The greater number and area of the corrosion pits on the surface are, the worse the pitting resistance is. To quantify the pitting resistance, the pitting areas were statistically analysed. The proportion of corrosion pits in the total area of the sample is defined as f_{pitting}. As can be seen from Fig. 10, the values of f_{pitting} of PA, RRA and RRRA samples are 4.04%, 2.48% and 3.78%, respectively. Hence, it is concluded that the pitting resistance follows the order of RRA > RRRA > PA samples.

The engineering stress−strain curves obtained from the SSRT tests in air and 3.5 wt.% NaCl solution are plotted in Fig. 11. The corresponding YS, UTS and elongation are listed in Table 4. The results indicate that the variations of YS, UTS, and elongation are basically the same as those measured from the ordinary tensile conditions. When the samples are subjected to 3.5 wt.% NaCl solution, the values of YS, UTS, and elongation are all obviously decreased.

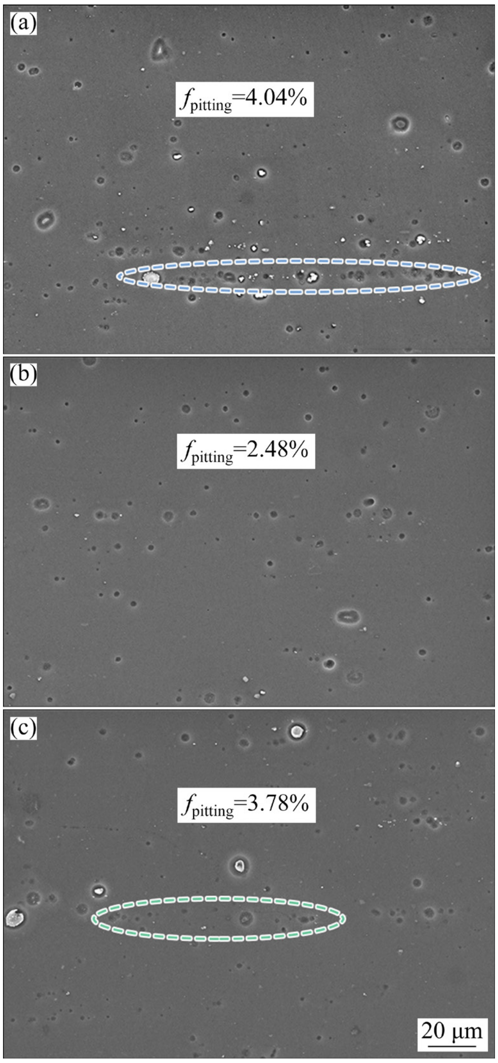

Fig. 10 SEM images of samples treated by PA (a), RRA (b), and RRRA (c) immersed in 3.5 wt.% NaCl aqueous solution for 24 h at room temperature

Table 4 lists the SCC sensitivity index (I_{scc}) of the aged samples, and I_{scc} can be calculated:

$$I_{\text{SCC}} = P_{\text{env}} / P_{\text{air}} \tag{6}$$

where P_{env} and P_{air} are the relevant parameters measured in solution and air respectively, including the elongation (ε), fracture energy (E_{F}) and fracture time (t). Based on the ratio of a certain parameter calculated by SSRT test in corrosive solution and air, correlation coefficients are used to evaluate SCC resistance. For example, $t_{\text{env}}/t_{\text{air}}$ coefficient is the ratio of the fracture time in corrosive solution to

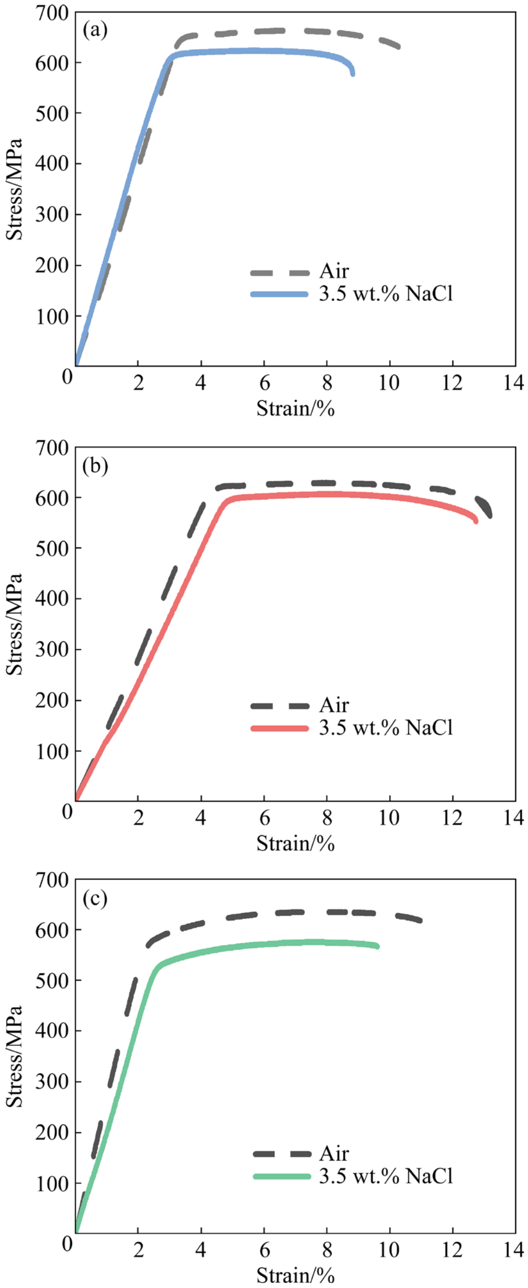

Fig. 11 Engineering stress−strain curves obtained from SSRT tests in air and 3.5 wt.% NaCl of samples treated by PA (a), RRA (b), and RRRA (c)

Table 4 Calculated I_{scc} values based on SSRT tests in air and 3.5 wt.% NaCl solution

Sample	Environment	SSRT data					SCC index		
		YS/ MPa	UTS/ MPa	Strain to fracture/%	Time to fracture/h	Fracture energy/($\mathrm{J \cdot cm^{-3}}$)	$\varepsilon_{\mathrm{env}}/\varepsilon_{\mathrm{air}}$	$t_{\mathrm{env}}/t_{\mathrm{air}}$	$E_{\mathrm{F,env}}/E_{\mathrm{F,air}}$
PA-treated	Air	638	662	10.67	61.8	58.8	82.5	82.7	77.4
	NaCl	590	624	8.81	51.1	45.5			
RRA-treated	Air	602	627	13.18	61.0	68.1	96.7	96.6	90.0
	NaCl	577	605	12.74	58.9	61.3			
RRRA-treated	Air	588	634	11.1	56.5	55.5	86.5	88.8	84.6
	NaCl	539	574	9.6	50.2	46.4			

the time in air. The larger the coefficient is, the better the SCC resistance is. As listed in Table 4, all the coefficients of RRA sample are the largest, indicating that RRA sample owns the best SCC resistance. However, PA sample has the lowest coefficient among these three samples, which means the worst SCC resistance. The coefficients of RRRA sample are somewhere between the above two samples.

Based on the SEM and TEM images, it is known that the second phases of the aged samples mainly include η', η, $\mathrm{Al_2CuMg}$ and $\mathrm{Al_7Cu_2Fe}$, all of which have different potentials to the nearby Al matrix [37]. When the alloy is placed in NaCl corrosive solution, the galvanic reaction occurs between the second phase and the matrix, which promotes the occurrence of pitting corrosion. Due to the existence of coarse GBPs, the potential difference between the matrix and the precipitated phase enables the pitting corrosion to preferentially occur in PFZ, forming the intergranular corrosion along GB. Therefore, as shown in Fig. 10, the rows of continuous corrosion pits are observed. SARKAR et al [38] found that the increase of Cu content weakened the electrochemical activity of η phase, thereby slowing down the dissolution rate of the more noble precipitates. This means that the higher Cu content is, the higher the pitting resistance is. Based on the EDS mapping results shown in Fig. 7, it is reasonable that RRA and RRRA samples own better pitting resistance due to their higher Cu content in GBPs than the PA sample. The SCC resistance is also closely related to GBPs. Many literatures [39−41] revealed that the mechanism of SCC in Al−Zn−Mg alloy was attributed to the anodic dissolution and the hydrogen embrittlement. Under applied loading, the η phase acting as the anode will preferentially be dissolved and act as the crack initiation sites. The cracking path propagates along GB, which facilitates the intergranular crack [42]. In general, the stress corrosion rate is negatively correlated with the dissolution of η phase [43]. Hence, the initiation and propagation of cracks can be inhibited or delayed by the coarse and discontinuous η phase. As mentioned, the RRA sample has the largest precipitate size and inter-space of GBPs, which results in the best SCC resistance. The SCC resistance of PA and RRRA samples can also be explained based on the size and inter-space of GBPs.

4 Conclusions

(1) The precipitates of PA sample are mainly unstable η' phase with the finest size and densest distribution, while the coarse and the stable η phase is formed after RRA treatment. Due to the dislocations introduced by pre-rolling, the precipitate kinetics of RRRA sample is promoted, resulting in a smaller precipitate size.

(2) The PA sample owns extremely high hardness and strength due to the strong precipitation strengthening. Although both the hardness and strength of RRA and RRRA samples are reduced, RRRA sample always exhibits higher values.

(3) Due to the higher Cu content of GBPs, RRA and RRRA samples exhibit better pitting corrosion resistance than PA sample. Since the GBPs of RRA sample exhibit the largest size and inter-space, the best SCC resistance is obtained. The resistance of both pitting corrosion and SCC follows the order of RRA sample > RRRA sample > PA sample.

Acknowledgments

The authors would like to acknowledge the financial supports from the National Natural Science

Foundation of China (No. 52175338), the Science Fund for Distinguished Young Scholars of Shandong Province, China (No. ZR2021JQ21), and the Research Foundation of Nanjing Vocational University of Industry Technology, China (No. YK20-01-01).

References

[1] DURSUN T, SOUTIS C. Recent developments in advanced aircraft aluminium alloys [J]. Materials & Design, 2014, 56: 862−871.

[2] de SALVO J G, AFONSO C R. Fatigue strength and microstructure evaluation of Al 7050 alloy wires recycled by spray forming, extrusion and rotary swaging [J]. Transactions of Nonferrous Metals Society of China, 2020, 30: 3195−3209.

[3] PENG Ying-hao, LIU Chong-yu, WEI Li-li, JIANG Hong-jie, GE Zhen-jiang. Quench sensitivity and microstructures of high-Zn-content Al−Zn−Mg−Cu alloys with different Cu contents and Sc addition [J]. Transactions of Nonferrous Metals Society of China, 2021, 31: 24−35.

[4] SHAO Hong-bang, HUANG Yuan-chun, WANG Yan-ling. Effect of ageing process on microstructure, corrosion behaviors and mechanical properties of Al−5.6Zn−1.6Mg−0.05Zr alloy [J]. Journal of Central South University, 2022, 29: 1029−1040.

[5] DESCHAMPS A, LIVET F, BRÉCHET Y. Influence of predeformation on ageing in an Al−Zn−Mg alloy — I. Microstructure evolution and mechanical properties [J]. Acta Materialia, 1998, 47: 281−292.

[6] PARK J K, ARDELL A J. Microchemical analysis of precipitate free zones in 7075-A1 in the T6, T7 and RRA tempers [J]. Acta Metallurgica et Materialia, 1991, 39: 591−598.

[7] JI Yuan-yuan, XU Yun-ze, ZHANG Bin-bin, BEHNAMIAN Y, XIA Da-hai, HU Wen-bin. Review of micro-scale and atomic-scale corrosion mechanisms of second phases in aluminum alloys [J]. Transactions of Nonferrous Metals Society of China, 2021, 31: 3205−3227.

[8] RAO A U, VASU V, GOVINDARAJU M, SRINADH K S. Stress corrosion cracking behaviour of 7xxx aluminum alloys: A literature review [J]. Transactions of Nonferrous Metals Society of China, 2016, 26: 1447−1471.

[9] CINA B. Reducing the susceptibility of alloys, particularly aluminium alloys, to stress corrosion cracking: US patent, 3856584 [P]. 1974−12−24.

[10] PARK J K, ARDELL A J. Effect of retrogression and reaging treatments on the microstructure of Ai-7075-T651 [J]. Metallurgical Transactions A, 1984, 15: 1531−1543.

[11] WANG Ying-chen, LIU Mao-wen, XIAO Wen-long, ZHAO Wei-tao, MA Chao-li. Effects of multi-stage aging treatments on the precipitation behavior and properties of 7136 aluminum alloy [J]. Journal of Alloys and Compounds, 2020, 814: 152256.

[12] WANG Yi-chang, CAO Ling-fei, WU Xiao-dong, TONG Xin, LIAO Bin, HUANG Guang-jie, WANG Zhen-gan. Effect of retrogression treatments on microstructure, hardness and corrosion behaviors of aluminum alloy 7085 [J]. Journal of Alloys and Compounds, 2020, 814: 152264.

[13] ZHANG Jia-yi, WANG Bin, FENG Liang-dong. Comprehensive improvement of stress corrosion cracking resistance and strength by retrogression and re-aging in Al−8.9Zn−2.6Mg−1.7Cu alloy [J]. Journal of Alloys and Compounds, 2022, 893: 162310.

[14] DESCHAMPS A, BRÉCHET Y, GUYOT P, LIVET F. On the influence of dislocations on precipitation in Al−Zn−Mg alloy [J]. International Journal of Materials Research, 1997, 88: 601−606.

[15] LIN Liang-hua, LIU Zhi-yi, ZHUANG Wen-wei, PENG Hai-jian. Effects of pre-strain on the surface residual stress and corrosion behavior of an Al−Zn−Mg−Cu alloy plate [J]. Materials Characterization, 2020, 160: 110129.

[16] CERESARA S, FIORINI P. Resistometric investigation of the ageing process after quenching and cold-work in Al−Zn−Mg alloys [J]. Materials Science and Engineering, 1972, 10: 205−210.

[17] YUAN Ding-ling, CHEN Kang-hua, CHEN Song-yi, HUANG Lan-ping, CHEN Geng, CHEN Si-jun. Effect of pre-strain and quench rate on stress corrosion cracking resistance of a low-Cu containing Al−Zn−Mg−Cu alloy [J]. Materials Science and Engineering A, 2022, 833: 142374.

[18] WANG Dong, NI Ding-rui, MA Zong-yi. Effect of pre-strain and two-step aging on microstructure and stress corrosion cracking of 7050 alloy [J]. Materials Science and Engineering A, 2008, 494: 360−366.

[19] WANG Dong, MA Zong-yi, GAO Zhong-min. Effects of severe cold rolling on tensile properties and stress corrosion cracking of 7050 aluminum alloy [J]. Materials Chemistry and Physics, 2009, 117: 228−33.

[20] ZHANG Cun-sheng, ZHANG Zhao-gang, LIU Ming-fu, BAO En-cheng, CHEN Liang, ZHAO Guo-qun. Effects of single- and multi-stage solid solution treatments on microstructure and properties of as-extruded AA7055 helical profile [J]. Transactions of Nonferrous Metals Society of China, 2021, 31: 1885−1901.

[21] XU D K, ROMETSCH P A, BIRBILIS N. Improved solution treatment for an as-rolled Al−Zn−Mg−Cu alloy. Part I. Characterisation of constituent particles and overheating [J]. Materials Science and Engineering A, 2012, 534: 234−243.

[22] DUMONT M, LEFEBVRE W, DOISNEAU-COTTIGNIES B, DESCHAMPS A. Characterisation of the composition and volume fraction of η' and η precipitates in an Al−Zn−Mg alloy by a combination of atom probe, small-angle X-ray scattering and transmission electron microscopy [J]. Acta Materialia, 2005, 53: 2881−2892.

[23] THRONSEN E, MARIOARA C D, SUNDE J K, MINAKUCHI K, KATSUMI T, ERGA I, ANDERSEN S J, FRIIS J, MARTHINSEN K, MATSUDA K, HOLMESTAD R. The effect of heavy deformation on the precipitation in an Al−1.3Cu−1.0Mg−0.4Si wt.% alloy [J]. Materials & Design, 2020, 186: 108203.

[24] EMBURY J D, NICHOLSON R B. The nucleation of precipitates: The system Al−Zn−Mg [J]. Acta Metallurgica, 1965, 13: 403−417.

[25] NANDANA M S, UDAYA BHAT K, MANJUNATHA C M. Effect of retrogression heat treatment time on microstructure and mechanical properties of AA7010 [J]. Journal of Materials Engineering and Performance, 2018, 27:

1628−1634.

[26] BAKKER H, BONZEL H P, BRUFF C M, DAYANANDA M A, GUST W, HORVATH J, KAUR I, KIDSON G V, LECLAIRE A D, MEHRER H, MURCH G, NEUMANN G, STOLICA N, STOLWIJK N A. Diffusion in solid metals and alloys [M]. Berlin: Springer, 1990.

[27] GHOSH A, GHOSH M, SEIKH A H, ALHARTHI N H. Phase transformation and dispersoid evolution for Al−Zn−Mg−Cu alloy containing Sn during homogenisation [J]. Journal of Materials Research and Technology, 2020, 9: 1−12.

[28] ZHAO Huan, de GEUSER F, de SILVA A K, SZCZEPANIAK A, GAULT B, PONGE D, RAABE D. Segregation assisted grain boundary precipitation in a model Al−Zn−Mg−Cu alloy [J]. Acta Materialia, 2018, 156: 318−329.

[29] FANG Xu, SONG Min, LI Kai, DU Yong, ZHAO Dong-dong, JIANG Chao, ZHANG Hong. Effects of Cu and Al on the crystal structure and composition of η ($MgZn_2$) phase in over-aged Al−Zn−Mg−Cu alloys [J]. Journal of Materials Science, 2012, 47: 5419−5427.

[30] BARDEL D, PEREZ M, NELIAS D, DESCHAMPS A, HUTCHINSON C R, MAISONNETTE D, CHAISE T, GARNIER J, BOURLIER F J. Coupled precipitation and yield strength modelling for non-isothermal treatments of a 6061 aluminium alloy [J]. Acta Materialia, 2014, 62: 129−140.

[31] DESCHAMPS A, BRECHET Y. Influence of predeformation and ageing of an Al−Zn−Mg alloy—II. Modeling of precipitation kinetics and yield stress [J]. Acta Materialia, 1998, 47: 293−305.

[32] SHERCLIFF H R, ASHBY M F. A process model for age hardening of aluminium alloys—I. The model [J]. Acta Metallurgica et Materialia, 1990, 38: 1789−1802.

[33] FLEISCHER R L. Solution hardening by tetragonal distortions: Application to irradiation hardening in FCC crystals [J]. Acta Metallurgica, 1962, 10: 835−842.

[34] FLEISCHER R L. Substitutional solution hardening [J]. Acta Metallurgica, 1963, 11: 203−209.

[35] MA K, WEN Hai-ming, HU Tao, TOPPING T D, ISHEIM D, SEIDMAN D N, LAVERNIA E J, SCHOENUNG J M. Mechanical behavior and strengthening mechanisms in ultrafine grain precipitation-strengthened aluminum alloy [J]. Acta Materialia, 2014, 62: 141−155.

[36] NEMBACH E. Particle strengthening of metals and alloys [M]. New York: Wiley, 1997.

[37] BIRBILIS N, BUCHHEIT R G. Electrochemical characteristics of intermetallic phases in aluminum alloys: An experimental survey and discussion [J]. Journal of the Electrochemical Society, 2005, 152: B140.

[38] SARKAR B, MAREK M, STARKE E A. The effect of copper content and heat treatment on the stress corrosion characteristics of Al−6Zn−2Mg−X Cu alloys [J]. Metallurgical Transactions A, 1981, 12: 1939−1943.

[39] NAJJAR D, MAGNIN T, WARNER T J. Influence of critical surface defects and localized competition between anodic dissolution and hydrogen effects during stress corrosion cracking of a 7050 aluminium alloy [J]. Materials Science and Engineering A, 1997, 238: 293−302.

[40] SONG Reng-guo, DIETZEL W, ZHANG Baojing-Jin J, LIU Wei-jie, TSENG M K, ATRENS A. Stress corrosion cracking and hydrogen embrittlement of an Al−Zn−Mg−Cu alloy [J]. Acta Materialia, 2004, 52: 4727−4743.

[41] DENG Ying, PENG Bing, XU Guo-fu, PAN Qing-lin, YE Rui, WANG Ying-jun, LU Li-ying, YIN Zhi-min. Stress corrosion cracking of a high-strength friction-stir-welded joint of an Al−Zn−Mg−Zr alloy containing 0.25 wt.% Sc [J]. Corrosion Science, 2015, 100: 57−72.

[42] DUX E H. Acceleration of the rate of corrosion by high constant stresses [J]. Transactions of the American Institute of Mining and Metallurgical Engineers, 1940, 137: 11−40.

[43] ROUT P K, GHOSH K S. Effect of microstructural features on stress corrosion cracking behaviour of 7017 and 7150 aluminium alloy [J]. Materials Today: Proceedings, 2018, 5: 2391−2400.

复合预轧制与回归再时效平衡 7A99 铝合金的强度和耐蚀性

张 涛[1]，侯玉柱[2]，阙标华[2]，田育鑫[3]，陈 良[2]

1. 南京工业职业技术大学 机械工程学院，南京 210023；
2. 山东大学 材料液固结构演变与加工教育部重点实验室，济南 250061；
3. 山东工商学院 计算机科学与技术学院，烟台 264005

摘 要：对 7A99 铝合金分别进行峰值时效(PA)和回归再时效(RRA)处理，并复合预轧制与回归再时效(RRRA)以平衡其力学性能和耐腐蚀性能。结果表明，PA 处理的试样析出物主要是尺寸细小的不稳定 η'相，而经 RRA 和 RRRA 处理后则出现粗大稳定的 η 相。PA 处理的试样晶界析出物尺寸最小且呈连续分布，而经 RRA 和 RRRA 处理后，晶界析出物的尺寸增大、分布不连续，并发生铜富集。RRRA 处理的试样硬度和强度均高于 RRA 处理的试样，甚至接近 PA 处理的试样。此外，试样经 RRA 和 RRRA 处理后，表现出比 PA 试样更好的抗腐蚀能力。这些结果表明，提出的预轧制和回归再时效方法能够在不大幅削弱强度的情况下提高合金的耐腐蚀性。

关键词：7A99 铝合金；时效；预轧制；析出相；力学性能；耐蚀性

(Edited by Bing YANG)